

A pre-stack migration method for damage identification in composite structures

L. Zhou[†]

*College of Aerospace Engineering, Nanjing University of Aeronautics and Astronautics,
Nanjing 210016, China*

F. G. Yuan[‡]

*Department of Mechanical and Aerospace Engineering, North Carolina State University,
Raleigh, NC 27695-7921, USA*

W. J. Meng^{‡†}

*College of Aerospace Engineering, Nanjing University of Aeronautics and Astronautics,
Nanjing 210016, China*

(Received March 2, 2006, Accepted January 2, 2007)

Abstract. In this paper a damage imaging technique using pre-stack migration is developed using Lamb (guided) wave propagation in composite structures for imaging multi damages by both numerical simulations and experimental studies. In particular, the paper focuses on the experimental study using a finite number of sensors for future practical applications. A composite laminate with a surface-mounted linear piezoelectric ceramic (PZT) disk array is illustrated as an example. Two types of damages, one straight-crack damage and two simulated circular-shaped delamination damage, have been studied. First, Mindlin plate theory is used to model Lamb waves propagating in laminates. The group velocities of flexural waves in the composite laminate are also derived from dispersion relations and validated by experiments. Then the pre-stack migration technique is performed by using a two-dimensional explicit finite difference algorithm to back-propagate the scattered energy to the damages and damages are imaged together with the excitation-time imaging conditions. Stacking these images together deduces the resulting image of damages. Both simulations and experimental results show that the pre-stack migration method is a promising method for damage identification in composite structures.

Keywords: damage detection; pre-stack migration; Lamb wave; composite; Mindlin plate theory; structural health monitoring.

1. Introduction

In aerospace and mechanical engineering, even in civil engineering, critical regions in structures need continual and on-line diagnosis of detecting and locating the damage in a structure and then of

[†]Professor, Corresponding author, E-mail: lzhou@nuaa.edu.cn.

[‡]Professor, E-mail: yuan@ncsu.edu

^{‡†}Graduated Student, E-mail: m_weijie@nuaa.edu.cn

quantitatively assessing its severity. Structural health monitoring system (SHMS) has promising potential in enhancing the performance and safety and reducing maintenance cost (Boller 2000). Over the past thirty years, research on the migration method has attained a maturity and is indispensable as an advanced interpretation method for reflection wavefield in geophysical exploration and seismic data analysis (e.g., Claerbout 1985). Essentially the migration technique is to reverse the scattered wavefield and to image the Earth interior. It potentially offers a promising method to fulfill active, in-service damage identification in SHMS.

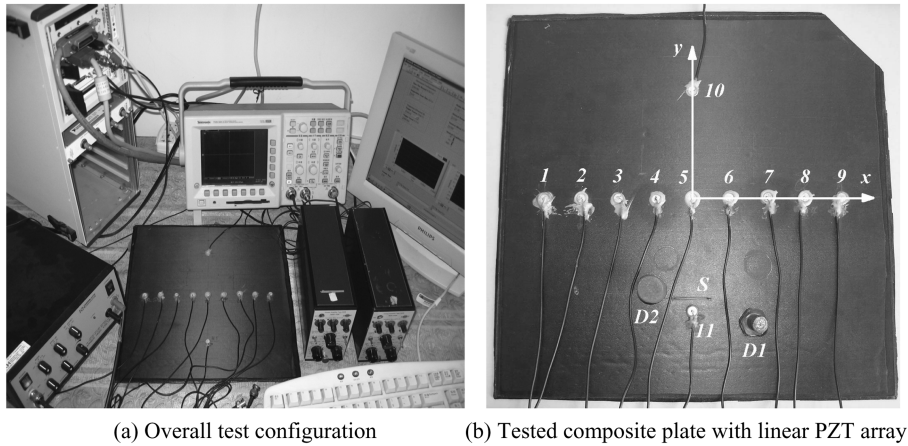
However, until recently few researches have been focused on the migration method applied in SHMS for damage imaging. It was firstly demonstrated that the migration method could be applied in the NDE for concrete structures with surface-breaking cracks (Liu, *et al.* 1996). The migration technique was also employed to correctly image a square-shaped damage in an aluminum plate through numerical simulation (Lin and Yuan 2001a). While these studies were based on post-stack migration in which migration was performed after the stacking process, the disadvantage is obvious in that post-stack migration cannot accurately image dipped damages where the surface of the damage is not parallel to the sensor array. A pre-stack reverse-time migration was introduced to visualize two arbitrary small damages in an aluminum plate by numerical simulation (Lin and Yuan 2001b), and then imaged an arc-shaped crack through experiments using PZT as actuators and sensors alternately (Lin and Yuan 2001c, 2005). Almost all of the previous studies were validated in theory and experiments for metallic isotropic materials. Very recently the pre-stack reverse-time migration was applied to visualize two arbitrary small damages in a composite laminate and validated it by numerical simulation (Wang and Yuan 2005). However, the experimental application using pre-stack reverse-time migration to composite structures has not yet been examined.

The objective of this study is to image multiple damages in a composite laminate by numerical simulations and experimental studies using ultrasonic Lamb waves with pre-stack reverse-time migration method. This work is an extension from a previous work (Wang and Yuan 2005). A composite laminate with a surface-mounted linear piezoelectric ceramic (PZT) disk array is illustrated as an example. Two types of damages have been studied, including one straight-crack damage and two simulated circular-shaped delamination damages.

2. Experimental setup

The overall test configuration in this study is shown in Fig. 1(a). The test setup consists of a composite laminate with a surface-mounted linear PZT sensor array, a NI PXI-based data acquisition (DAQ) system incorporated with a NI PXI-8176 embedded controller, a NI PXI-5411 arbitrary function generator and NI LabVIEW software, a Krohn-Hite Model 7602 Power Amplifier, two Brüel & Kjær Type 2635 Charge Amplifiers, and a Tektronix TDS3012 Digital Oscilloscope.

Fig. 1(b) shows the composite laminate with the linear PZT array. A symmetric $[0_3/-45/45/0_3/-45/45_2]_s$ graphite/epoxy phenolic resin T300/648 laminate is selected for illustration. The plate dimension is 300 mm×300 mm×2.1 mm. Fiber volume fraction is around 65% and the material properties for the composite are listed in Table 1. The subscripts 1, 2, and 3 refer to principal material axes along fiber, transverse, and thickness direction respectively. The origin of the coordinate system is set at the center of the plate. For practical applications, the linear sensor array consists of nine PZT sensors (diameter: 8mm, thickness: 1 mm), denoted by 1, 2,..., 9 for damage imaging. These nine PZT sensors are distributed along the x -axis from (-120 mm, 0 mm) to (120 mm, 0 mm) with spacing 30 mm. These



(a) Overall test configuration (b) Tested composite plate with linear PZT array
Fig. 1 An experimental built-in damage identification system

Table 1 Properties of T300/648 lamina (fiber volume fraction = 65%)

E_1 (GPa)	E_2 (GPa)	E_3 (GPa)	G_{12} (GPa)	G_{23} (GPa)	G_{13} (GPa)	ν_{12}	ν_{13}	ρ (Kg/m ³)
125.44	7.947	7.947	4.748	4.092	4.748	0.33	0.33	1587.9

nine sensors also act as actuators alternately. The PZT10 and PZT 11 are used to excite the signals and the nine PZT sensors collected the sensor signal for group velocity evaluation. Each actuator excites a transient diagnostic wave in the composite laminate. The traces, which are collected by all of the remaining sensors, assemble the time section data record to reconstruct the response wavefield. The wavefield solely reflected from the damages can be obtained by subtracting the wavefield without damage from that with damage. For the first damage type, one straight-crack, marked with S , is chamfered through the plate with dimensions 30 mm \times 1 mm and its center location is at (0 mm, -80 mm). For the second damage type, two steel nuts with diameter 20 mm, marked with D1 and D2, are used to mount on the surface of the tested composite laminate by high strength glue to simulate circular-shaped delaminations respectively. The center of two damages are located at (47 mm, -96 mm) and (-30 mm, -75 mm) respectively.

3. Wave propagation in composite laminate

3.1. Dispersive relations in composites

It has been shown that the approximate solution from Mindlin plate theory (MPT) provides accurate results for the lowest mode of flexural waves (Lih and Mal 1995(a), 1995(b)). In this study, MPT, which takes into account the effects of transverse shear deformation and rotary inertia, is adopted to model the flexural waves propagating in a thin composite laminate. The dispersive relations of different wave modes propagating along various directions in the composite laminate can be calculated according to the reference (Wang and Yuan 2005). The phase and group velocities along the 0° direction are shown in Fig. 2 and Fig. 3. It is noticed based on MPT that the S_0 and SH_0 modes are non-dispersive and the

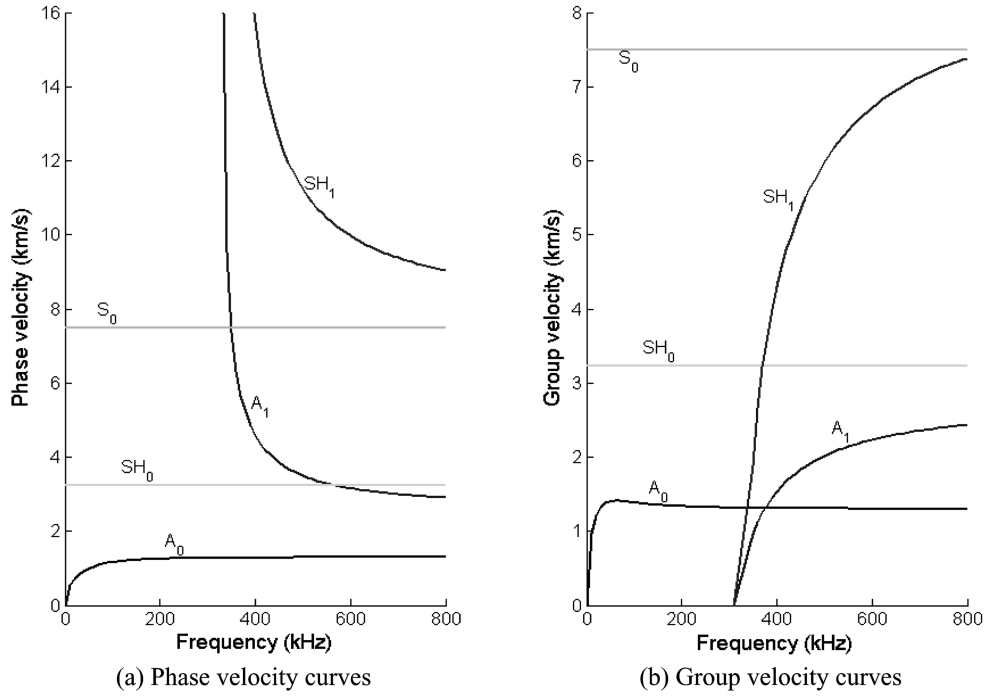


Fig. 2 Dispersion curves for waves propagating along 0° direction

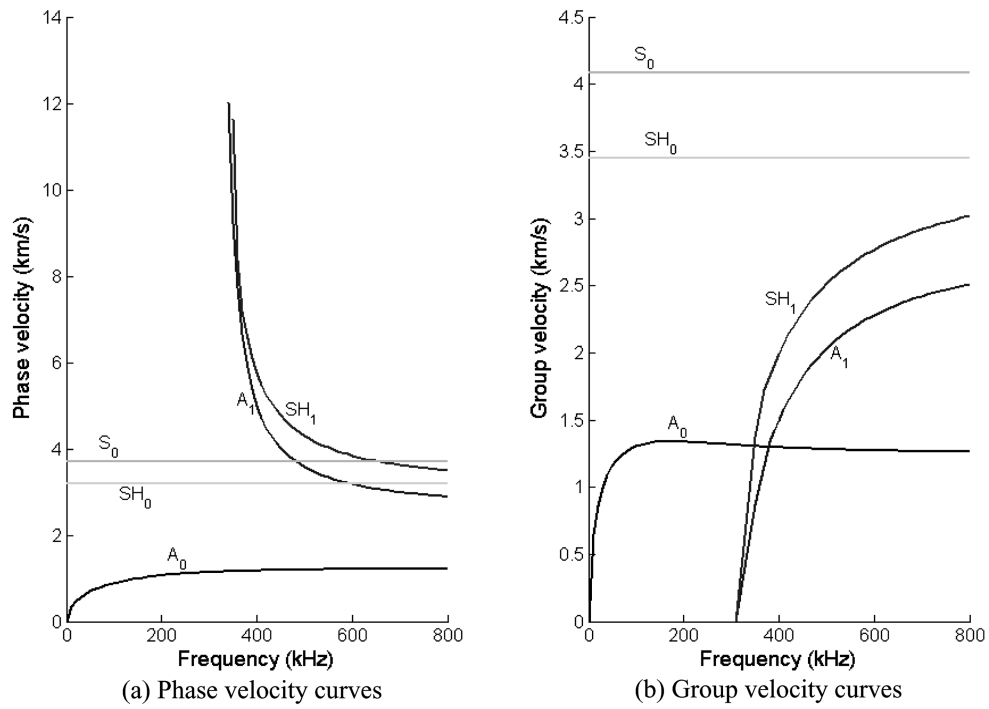


Fig. 3 Dispersion curves for waves propagating along 90° direction

tail region of the A_0 mode in the moderately high frequency range are relatively flat, thus the dispersive effect in these ranges is insignificant. Although the S_0 mode of extensional wave is ideal for SHM, it was difficult to work with such mode in practice because this mode signal is very weak and attenuates quickly (Sohn, *et al.* 2004). The SH_0 wave is not applicable as a result of utilizing d_{31} phenomenon of the PZT sensor. In addition, beyond the cut-off frequencies, A_1 and SH_1 indicate significantly dispersive effect. Fig. 3 shows the dispersion curves of different modes in the composite laminate propagating along the 90° direction. A similar phenomenon of these wave modes could be observed. In this paper the lowest flexural A_0 wave mode is selected as the diagnostic signal for imaging the damage. The dispersion relationships and the group velocities of A_0 wave mode will be validated by experiments at Section 6.1.

3.2. Governing equations

In order to simplify governing equation for the A_0 flexural waves using MPT, define two new vectors

$$\mathbf{u} = [\dot{w}, \dot{\psi}_x, \dot{\psi}_y, Q_x, Q_y, M_x, M_y, M_{xy}]^T \text{ and } \mathbf{q} = [q, 0, 0, 0, 0, 0, 0, 0]^T$$

where \dot{w} , $\dot{\psi}_x$, $\dot{\psi}_y$ represents the transverse displacement, rotation with respect to y and x axes respectively; Q_x and Q_y are transverse shear force per unit length acting on the cross section along the x and y directions respectively; M_x , M_y , and M_{xy} are the bending moments per unit length with respect to y and x axes and twisting moment per unit length respectively. q is the transverse force per unit area. Then the governing equation can be expressed as a first-order equation in a matrix form

$$\frac{\partial \mathbf{U}}{\partial t} = \mathbf{A}_t \frac{\partial \mathbf{U}}{\partial x} + \mathbf{B}_t \frac{\partial \mathbf{U}}{\partial y} + \mathbf{C}_t \mathbf{U} + \mathbf{q} \quad (1)$$

where $\mathbf{U} = \mathbf{E}_0 \mathbf{u}$, $\mathbf{A}_t = \mathbf{A}_0 \mathbf{E}_0^{-1}$, $\mathbf{B}_t = \mathbf{B}_0 \mathbf{E}_0^{-1}$, $\mathbf{C}_t = \mathbf{C}_0 \mathbf{E}_0^{-1}$. \mathbf{A}_0 , \mathbf{B}_0 , \mathbf{C}_0 , and \mathbf{D}_0 are matrices listed in Lin and Yuan (2001a) and, thus, are not repeated here. Since the damage area is considered as a region of inhomogeneity in the laminate, only the property matrix \mathbf{E}_0 needs to be altered in the governing equation, which will make the modeling of reflected wave from damages much easier in the numerical calculation (Wang and Yuan 2005).

3.3. Finite difference algorithm

A 2-6-order finite difference algorithm (second-order accuracy in time and sixth-order accuracy in space) is employed in this study to simulate the lowest-order flexural wave propagating in a composite plate (Wang and Yuan 2005). Consider the major portion of Eq. (1)

$$\frac{\partial \mathbf{U}}{\partial t} = \mathbf{A}_t \frac{\partial \mathbf{U}}{\partial x} + \mathbf{B}_t \frac{\partial \mathbf{U}}{\partial y} \quad (2)$$

The MacCormack splitting method can be expressed as the following compact form

$$\mathbf{U}^{n+2} = F_x F_y F_y^+ F_x^+ \mathbf{U}^n \quad (3)$$

where \mathbf{U}^n is the output value of the n^{th} time step and \mathbf{U}^{n+2} is for the $(n+2)^{\text{th}}$ time step. F_x , F_x^+ , F_y , and F_y^+ are the backward-forward operators and forward-backward operators in the x , y directions respectively.

Each operator processes the calculation by a half time step; thus a complete update of Eq. (3) includes four operators in two time steps. In each sequential time step, the order of the x, y direction updates is reversed, so is the order of forward-backward and back-forward operators.

For the term $\partial \mathbf{U} / \partial t = \mathbf{C}_t \mathbf{U}$ in Eq. (1), the increment of \mathbf{U} due to \mathbf{C}_t is calculated in advance by using $\Delta \mathbf{U}_{ij}^{(n)} = \exp(\mathbf{C}_t \Delta t)$ and then at each time step this term is added into each grid point. This method avoids the difference computation at each time step thus speeds up the calculation. For a point force with amplitude P , which is used in this study, the force term \mathbf{q} with $q = P/\Delta a$ is applied as a distributed force on a very small area Δa to simulate the loading. Because the last two terms in the right hand side of Eq. (1) are independent of spatial grid, they are updated after the splitting computation of Eq. (2) and summed into the result for each time step.

4. Imaging damages by pre-stack migration

For a distributed linear array actuator/sensor system, each actuator excites the lowest mode of transient flexural incident waves A_0 with the same waveform into the structures. All sensors collect the back-scattered waves, and sensor data are assembled as a time section. In the following, there steps in performing prestack reverse-time migration for imaging the damage(s) is briefly described.

4.1. Excitation-time imaging condition

The excitation–time imaging condition is employed in this study (Chang and McMechan 1986). The imaging condition is based on a concept that if both the incident wave and the reflected wave are extrapolated, the damages exist at the places where these two waves are in phase to each other. According to this condition, a grid point is imaged at its excitation-time when this point is excited at this time by the incident energy traveled from the actuator. This imaging condition is explicit, and each point in the image space has its own image time. Therefore, at each reverse time step $i\Delta t$, imaging is processed on the entire grid points and those points located on a locus defined by

$$t_d = (N - i + 1)\Delta t, \quad i = 1, 2, 3, \dots, N + 1 \quad (4)$$

where t_d is the direct (physical) time arrival from the actuator to the points, N is the maximum time step index, and Δt is the time step of the finite difference algorithm.

The imaging condition locus for each extrapolation time step can be computed prior to the reverse-time migration and is used as a reference table in the upcoming migration process.

4.2. Reverse-time extrapolation of reflected wavefield and application of imaging condition

The finite difference algorithm is used for reverse-time migration. The time section is now reversed with respect to time. Reverse-time extrapolation is a boundary-value problem of the transverse deformation velocity \dot{w} in which the finite difference mesh is driven with the time reverse of the trace received at each sensor. At each finite difference time step, new boundary values are extracted along a constant time slice through the sensor data and inserted at the corresponding sensor locations. In practical applications, the time step for migration is equal to the sampling interval of the A/D device. As time moves backwards, the reflected energy originating from the damages will focus back to the boundary of

the damages, pass through and then defocus (Wang and Yuan 2005).

At each extrapolation step of applying the imaging condition, the points on which the imaging condition locus crosses with the back-propagating wave front are imaged in terms of the velocity of the transverse deformation \dot{w} .

4.3. Stacking the images

When time back-propagates to zero, the reverse-time migration process is completed and the reflected energy may be imaged at the damage boundaries. However, some portions of the damage may not be imaged because the incident wave scattered from this damage site are not collected by the sensor array. Due to the finite area of the damage and the existence of the multiple damages, only a single reverse-time migration from one actuator is not sufficient to image all areas of the damages. Accordingly, exciting the waves from different actuators and producing the images of multiple damages is needed. Then, images from all the actuators are stacked; in this way, the signal-to-noise ratio of final image resolution of the multiple damages can be enhanced.

5. Numerical simulation

5.1. Synthesized reflected wavefield with damages

The graphite/epoxy phenolic resin T300/648 symmetric laminate described in Section 2 is modeled in this section. Two types of damages have been studied respectively, including one straight-crack damage and two simulated circular-shaped delamination damages. The one straight crack S and two small steel nuts $D1$ and $D2$ shown in Fig. 1(b) are modeled as damages separately. The signals that received from the linear array sensors by excitation of incident wave from the actuator arise from waves scattered from the damages and reflected from plate edges. The wavefield solely reflected from the damages can be obtained by subtracting the wavefield without damage from that with damages. To generate the sensor data along the linear array from the simulated reflected wavefield using forward finite difference algorithm, the damaged plate is considered as a plate with inhomogeneity; each damage region is modeled as an area of the plate with modified material properties. With this approach, the boundary conditions at the interfaces between the undamaged area and damages are implicitly satisfied. A 200×200 finite difference mesh ($\Delta x = \Delta y = 1.5$ mm) is superimposed on the plate region (300 mm \times 300 mm). The time step Δt is chosen as 0.1 msec. The total time span is 450 msec.

The excitation of transient waves from an actuator is a Hanning window modulated sinusoid transverse loading governed by

$$q(t)\Delta a = P[H(t) - H(t - N_p/f_c)] \times [1 - \cos(2\pi f_c t/N_p)] \sin(2\pi f_c t) \quad (5)$$

where $\Delta a = \Delta x \times \Delta y$, $H(t)$ is the Heaviside step function, P is the amplitude of the excitation force, N_p is the number of peaks of the loading, and f_c is the central frequency. The feature of this loading is that it has compact support in time domain (see Fig. 4(a)) and its frequency components concentrate at f_c in frequency domain (see Fig. 4(b)), thus the excited narrowband wave is relatively non-dispersive. Here, $N_p = 5$, $P = 1$ N and $f_c = 60$ kHz $< f_{cut-off} (= 309$ kHz) are chosen to ensure only the lowest mode of flexural waves propagating in the composite.

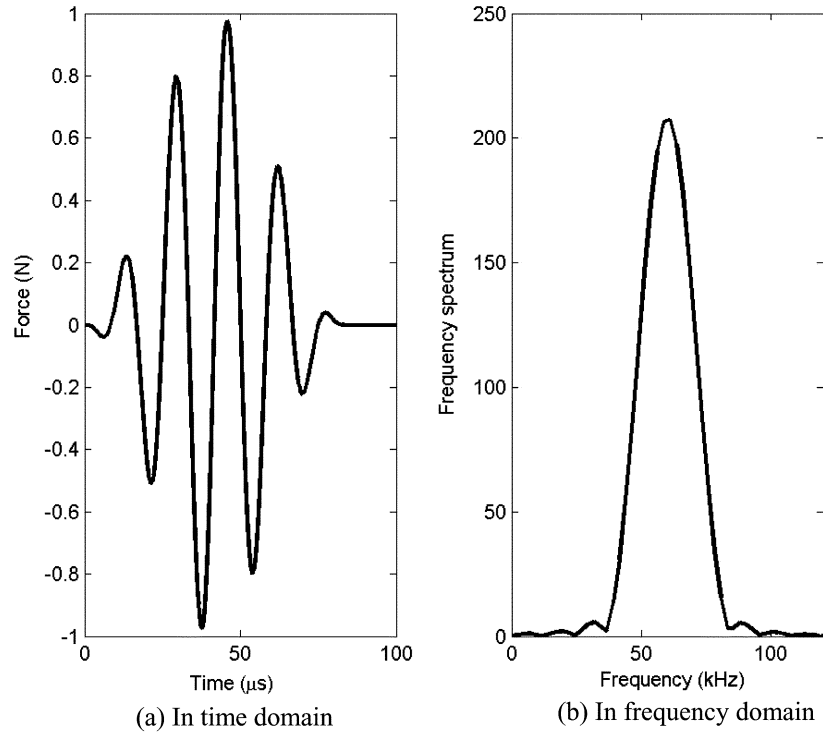


Fig. 4 Simulation excitation of transient waves at $f_c = 60$ kHz

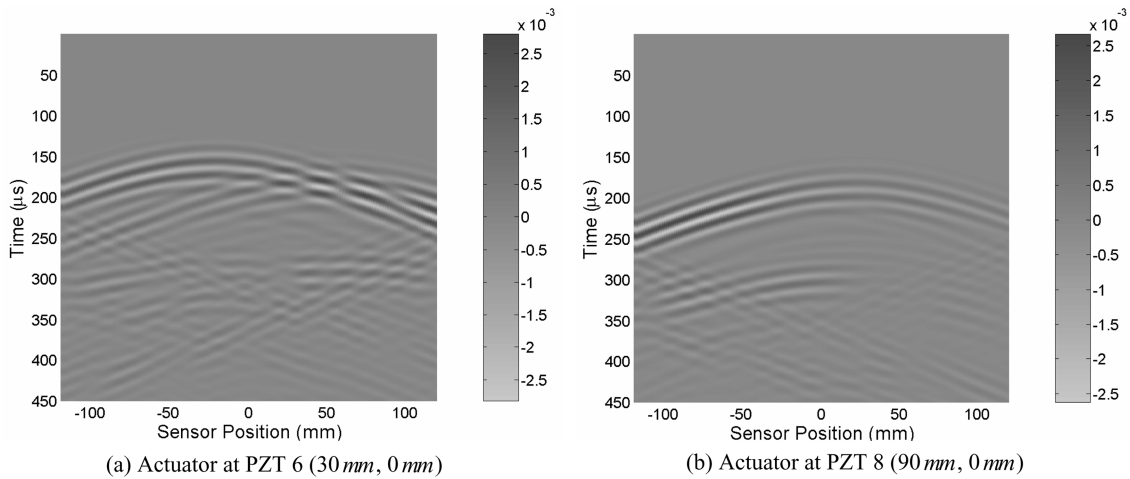


Fig. 5 Synthesized reflected wavefields \hat{w} scattered from one straight-crack damage

Fig. 5 displays the reflected wavefields of the one straight-crack damage in the form of time section, by exciting the signals at the PZT 6 (30 mm, 0 mm) and PZT 8 (90 mm, 0 mm) respectively. The abscissa represents the position of sensors located at $y=0$, which is the spatial grid point in the simulation where the waves are recorded. The ordinate represents the propagating time of the waves.

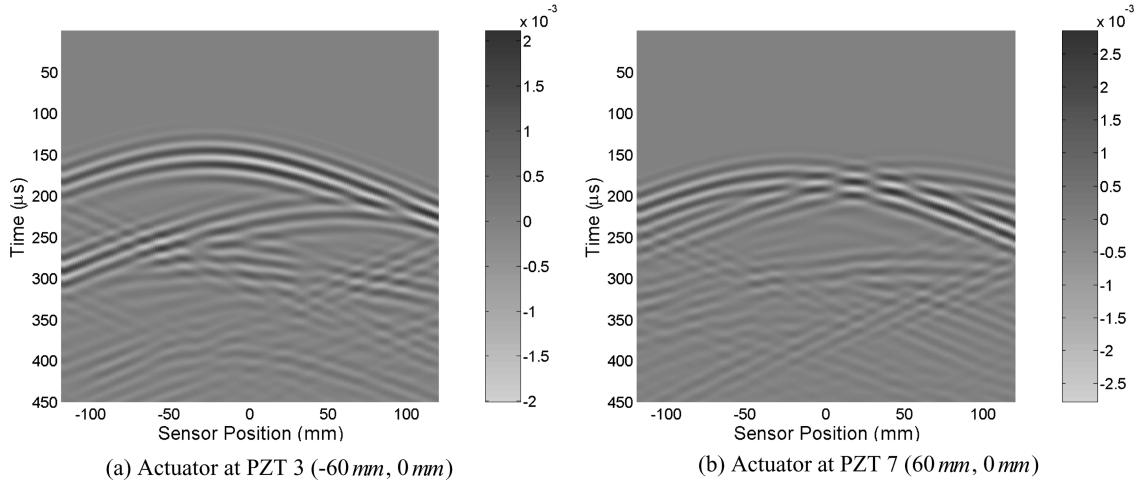


Fig. 6 Synthesized reflected wavefields \hat{w} scattered from two circular-shaped delamination damages

Each vertical line (a trace) is a time history of \hat{w} at the corresponding point. Note that the reflected wavefield from the damage is obtained by subtracting the wavefield without damage from the total reflected wavefield of the damaged plate. Fig. 6 displays the reflected wavefields of the two simulated circular-shaped delamination damage in the form of time section, by actuating the PZT 3 (-60 mm, 0 mm) and PZT 7 (60 mm, 0 mm) respectively. The coordinates are the same as Fig. 5 described above.

5.2. Numerical results

Fig. 7 gives two images of the one straight-crack damage by using migration without stacking. The plate is imaged by extracting the velocity of the transverse deformation \hat{w} at each grid point and is displayed in a plot with gray colormap. Fig. 7(a) is the image migrated from Fig. 5(a), i.e., excitation

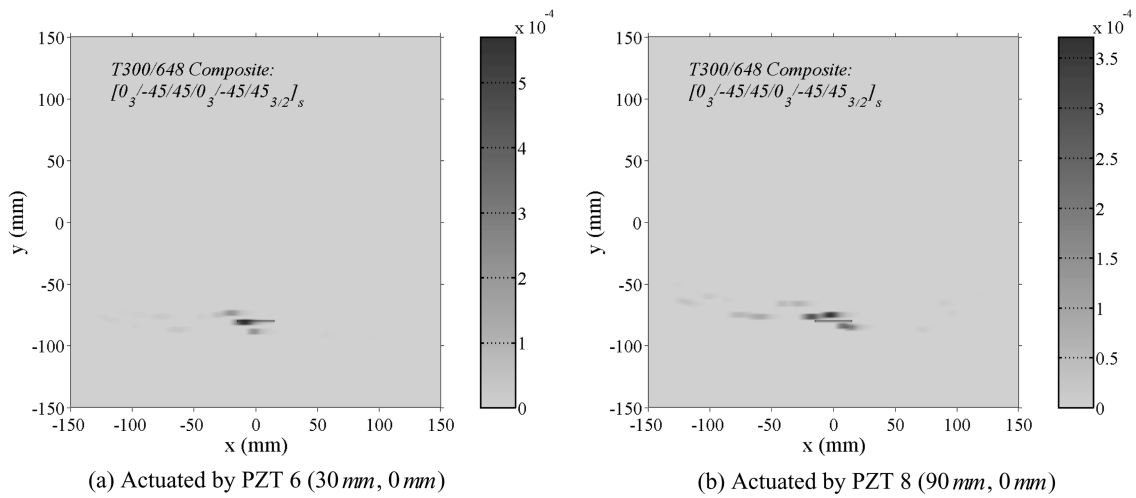


Fig. 7 Simulated images of one-straight crack damage by different actuators

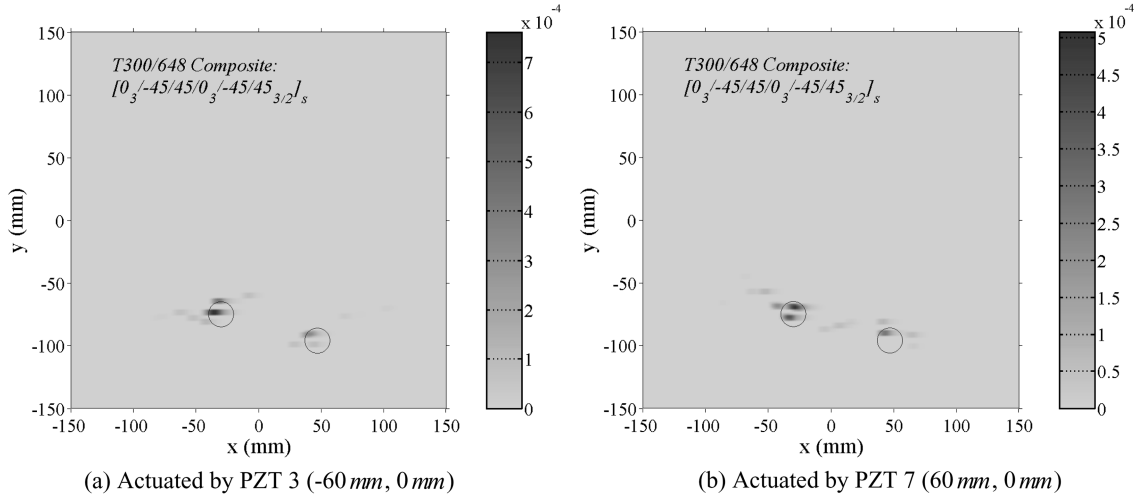


Fig. 8 Simulated images of two circular-shaped delamination damages by different actuators

generated by an actuator located at PZT 6 (30 mm, 0 mm). Fig. 7(b) displays the reverse-time pre-stack migration image from scattered wavefield in Fig. 5(b) with an actuator located at PZT 8 (90 mm, 0 mm). A shallow rectangle indicates the boundaries of the target damage. From the figures, it can be seen that the reverse-time migration successfully propagates the reflected energy back to the damage location, and imaging areas are clearly located at the boundaries of the target damages. From Fig. 7(a) and Fig. 7(b) it also shows that some artifacts occur near the target damage boundaries. The reason is that the incident waves from different actuators reach the different boundary portions of the crack damage, and then the reflected energy collected by the sensor array differs.

Fig. 8 gives images of the two simulated circular-shaped delamination damages by using migration. Fig. 8(a) is the image migrated from an excitation generated by an actuator located at PZT 3 (-60 mm, 0 mm). Fig. 8(b) displays the pre-stack migration image with an actuator located at PZT 7 (60 mm, 0 mm). Two circles indicate the boundaries of the target damages. From these figures, the same phenomena can be observed that imaging areas are clearly located at the boundaries of the target damages.

The final simulation stacking images of the two types of damages from the pre-stack migration images of seven actuators from PZT 2 (-90 mm, 0 mm) to PZT 8 (90 mm, 0 mm) with spacing 30 mm are shown in Fig. 9, respectively. All of the imaging areas are located mainly on the top boundaries of the target damages. In Fig. 9(a) the image gives the corresponding shape of one-straight-crack damage, while the majority of two circle-shaped damages can be clearly observed in Fig. 9(b).

6. Experiments

6.1. Validation of dispersion relationships

In the experimental study, the excitation of transient waves from an actuator is a Hanning window modulated sinusoid transverse loading which driven by voltage signal governed by the same function form in Eq. (5) where the force P is replaced by the voltage V .

Fig. 10 shows the group velocity curve of A_0 mode wave along the 90° direction of the symmetric

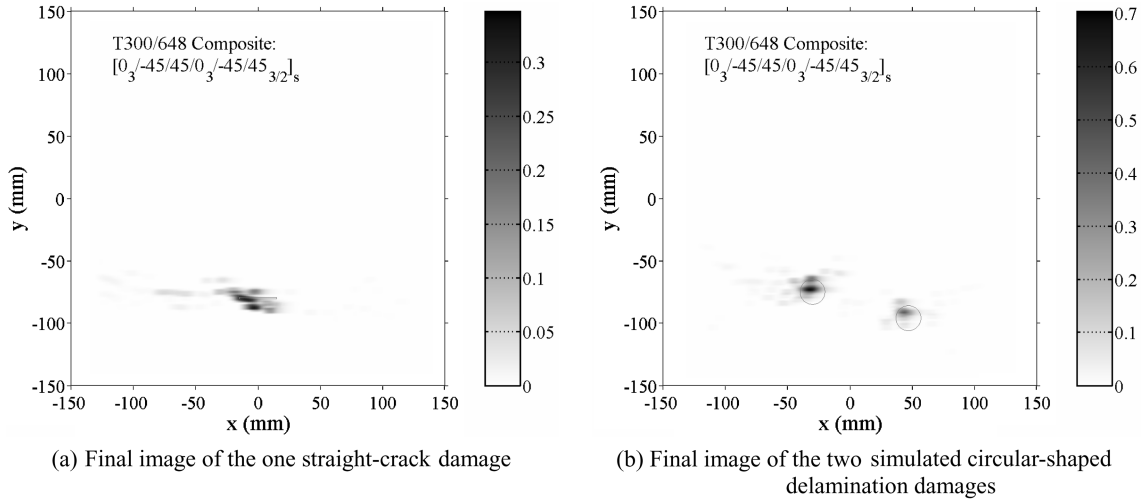


Fig. 9 The final simulation images of the two types of damages at $f_c = 60$ kHz

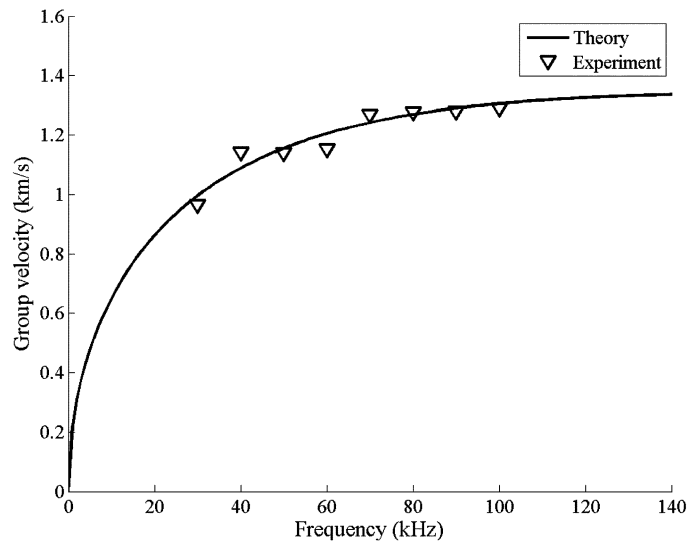


Fig. 10 Group velocity of A_0 wave along 90° direction

laminates calculated by MPT compared with experimental results. The group velocities are in good agreement with that based on MPT in the low frequency range. Therefore, wave behavior in the A_0 mode below the cut-off frequency can be accurately modeled by the MPT and used for the real SHMS. Here the flexural wave mode A_0 is chosen as diagnostic signal for migration. In this study, $N_p = 5$, $V = 56$ Volts and $f_c = 60$ kHz $< f_{cut-off}$ ($= 309$ kHz) are chosen to ensure only the lowest mode of flexural waves propagating in the composite plate. The wavelength of the central frequency is around 15 mm, half of the sensor spacing. Note that the sensor spacing does not satisfy the *spatial Nyquist sampling criterion*: the spacing should not be more than one-half of the minimum wavelength of the signal propagating in the structure. However a trade-off is made in this experimental study between resolution and incomplete spatial sampling of the data.

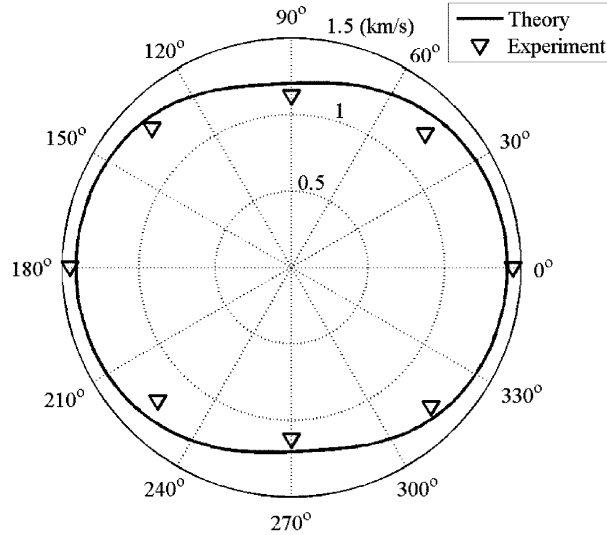


Fig. 11 Group velocity of A_0 wave at $f_c = 60$ kHz

Fig. 11 illustrates the velocity distributions \dot{w} of A_0 mode wave propagating in the test laminate. The velocities strongly depend on the direction of propagation due to the material anisotropy and layup. Experimental solution shows that it correlates well with theoretical result. Thus, it could provide the base information for constructing the excitation-time imaging condition.

6.2. Wavefield reconstruction

Fig. 12 shows the eight sensor voltage data. They are solely scattered signals from the one straight-crack damage actuated by PZT 5 located at the origin. The response wavefield on the grid points along

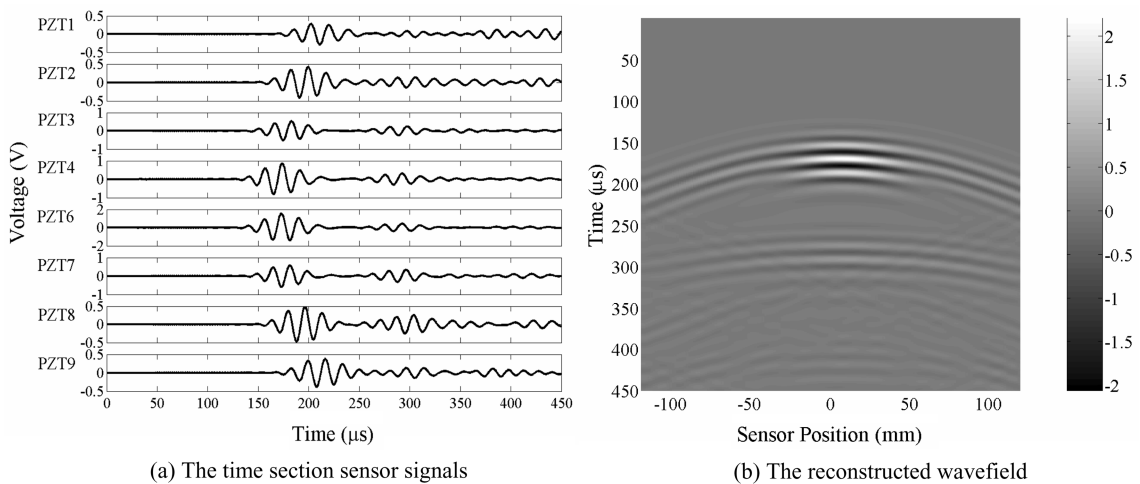


Fig. 12 Experimental eight sensor data scattered from one straight-crack damage actuated by PZT 5 (0 mm, 0 mm) at $f_c = 60$ kHz

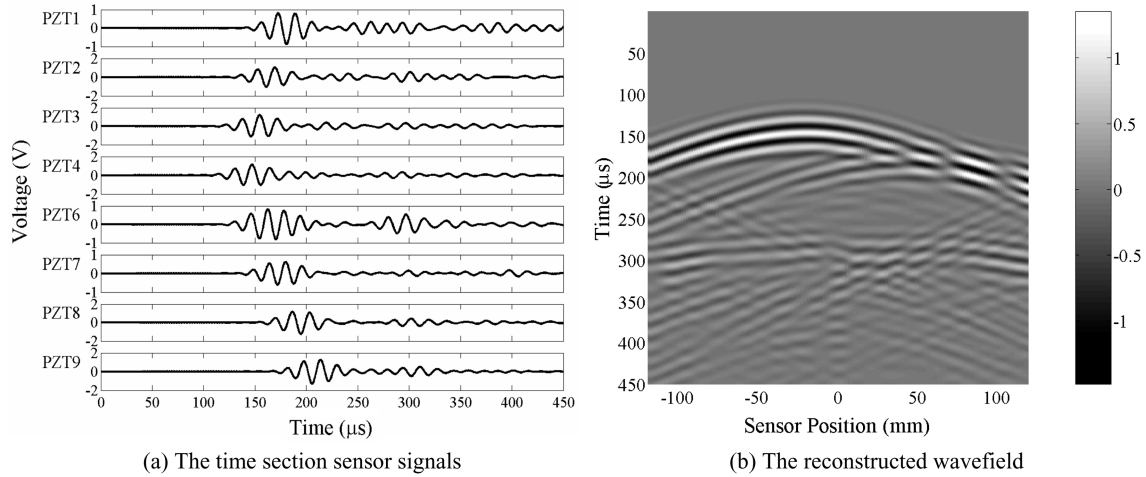


Fig. 13 Experimental eight sensor data scattered from the two simulated circular-shaped delamination damages actuated by PZT 5 (0 mm, 0 mm) at $f_c = 60$ kHz

the linear sensor array used in back-propagating waves in migration procedure can be formed by interpolation from this time section data. In this study, a fifth polynomial curve fitting through solving the least-squares problem is applied here for interpolation. Fig. 12(b) is the reconstructed reflection wavefield actuated by PZT 5, interpolated from Fig. 12(a). This reconstructed field in form of voltage signal could be directly applied for migration without translating into the velocity of the transverse deformation \dot{w} as studied in the numerical study.

Fig. 13 is the eight measured sensor data solely scattered from the two simulated circular-shaped delamination damages actuated by PZT 5 (0 mm, 0 mm). Similar to Fig. 12, the reconstructed time section in Fig. 13(b) is obtained from the measured sensor data in Fig. 13(a) by the fifth polynomial curve fitting processing.

6.3. Result of pre-stack migration

Same as in numerical simulation, the plate is discretized by a 200×200 finite difference mesh ($\Delta s = \Delta x = \Delta y = 1.5$ mm) for performing the migration procedure using the finite difference algorithm. The time interval Δt is chosen as 0.1 msec and time span is 450 msec.

In Fig. 14, two images of the one straight-crack damage generated by migration are shown. Fig. 14(a) is the image migrated from a single actuator generated by PZT 4 (-30 mm, 0 mm). Fig. 14(b) displays the migration image with PZT 5 located at (0 mm, 0 mm). Both of the two images show that the reverse-time migration successfully propagates the reflected energy back to the damage, and imaging areas are nearly located at the boundaries of the target damage although the sensor spacing does not satisfy the sampling theorem. However, migration of the reconstructed wavefield from a single actuator does not give a complete image of the damage. The reason is the same as in the numerical study discussed above, the incident waves from different actuators reach the different boundary portions of the damage.

Fig. 15 gives two images of the two simulated circular-shaped delamination damages generated by using migration, respectively. Fig. 15(a) is the image migrated from a single actuator generated by PZT 5 (0 mm, 0 mm). Fig. 15(b) displays the migration image with PZT 6 (30 mm, 0 mm). Both of the two images

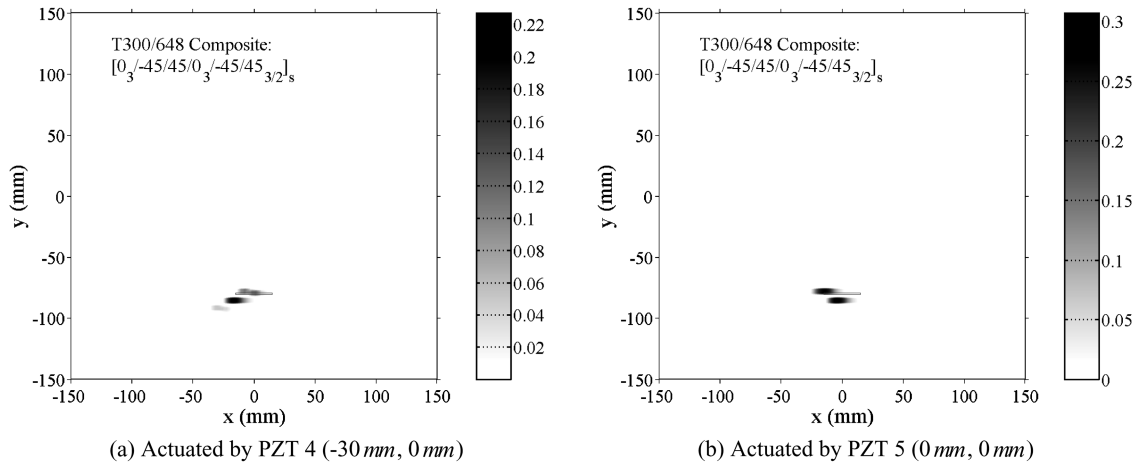


Fig. 14 The experimental images of one straight-crack by different actuators at $f_c = 60$ kHz

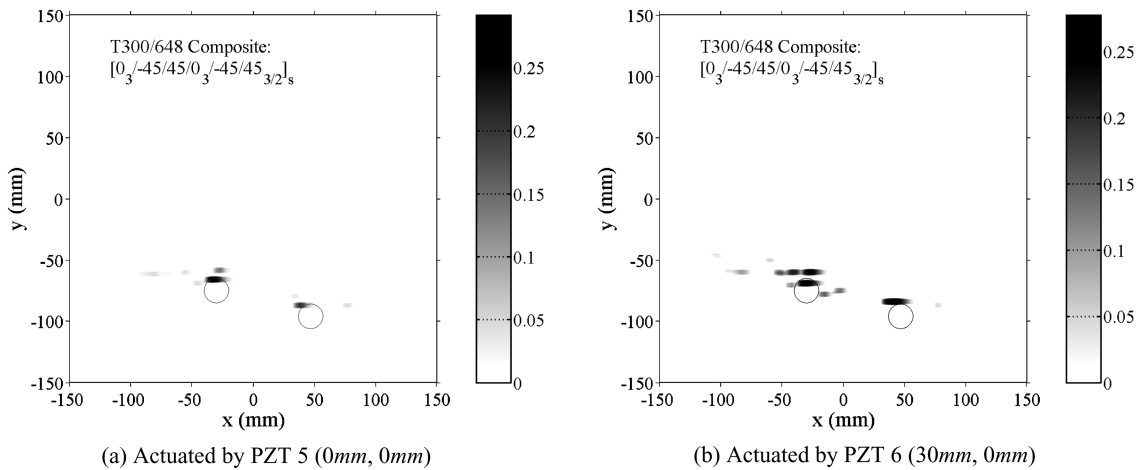


Fig. 15 The experimental images of two simulated circular-shaped delamination damages by different actuators at $f_c = 60$ kHz

illustrate that the imaging areas are nearly located at the boundaries of the two circular target damages.

Fig. 16 gives the final experimental stacking images of the two types of damages from the pre-stack reverse-time migration images of seven actuators, i.e., distributing from PZT 2 (-90 mm, 0 mm) to PZT 8 (90 mm, 0 mm) with spacing 30 mm. All of the imaging areas are located mainly on the boundaries of the target damages. In Fig. 16(a), the imaging areas are focused around the straight crack marked by rectangle lines, while the imaging areas in Fig. 16(b) focus at the two marked circles. Thus, the pre-stack reverse-time migration method is suitable for imaging multiple damages in the composite laminate. However, the images have some artifacts near the actual targeted damages. This might be due to the errors induced by the interpolation for reconstruction scattered wavefields. Besides, because the sensor array is placed above the damages, only the reflected energy from the upper portions of the damages can be collected and migrated to the damages. Thus the lower portions of the damages cannot be imaged.

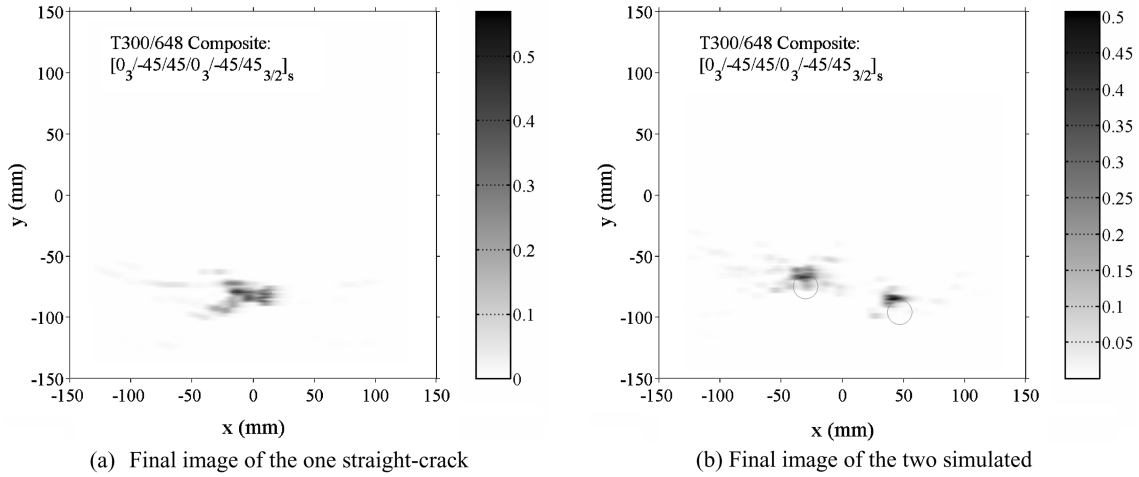


Fig. 16 The final experimental images of the two types of damages at $f_c = 60$ kHz

7. Conclusions

These numerical simulation and experimental studies demonstrate the ultrasonic Lamb wave-based pre-stack reverse-time migration as an advanced technique that can be used in an active SHM system. Based on the simulation results, the pre-stack migration method has successfully imaged the two types of damages in the composite plate. Through this experimental study using a finite number of sensors, it shows that the migration can effectively interpret the sensor data recorded by a distributed linear array sensor system and make it possible to establish an active, in-service and intelligent monitoring system for composite structures, although the sensor spacing does not satisfy the spatial Nyquist sampling theorem.

However, several limitations of the current approach should be paid attention. First, it is valid for thin composite laminates and the frequencies being relatively low because the wave model is based on approximate Mindlin plate theory. Second, due to the two-dimensional finite difference algorithm, the computational time cost is relatively high. In addition, an advanced interpolation algorithm needs to be developed such that the sensor spacing could be larger than the spacing of finite difference mesh, thus the time section could be constructed using a smaller number of sensors. Lastly, the linear array of actuators/sensors network distribution scheme should be optimized to image the entire areas of the target damages.

Acknowledgements

This research is partially supported by the National Natural Science Foundation of China under Grant No.50478037 and No.10572058, by the Science Foundation of Aeronautics of China under Grant No.04I52063, by the Research Fund for the Doctoral Program of Higher Education under Grant No.20050287016, and by the Scientific Research Foundation for the Returned Overseas Chinese Scholars, State Education Ministry. The authors also would like to appreciate the support from the National Science Foundation Grant No.CMS-0220027-01 for this US-China collaboration.

References

- Boller, C. (2000), "Next generation structural health monitoring and its integration into aircraft design", *Int. J. Sys. Sci.*, **31**(11), 1333-1349.
- Claerbout, J. F. (1985), *Imaging the Earth's Interior*, Blackwell Scientific Publications.
- Chang, W. F. and McMechan, G. A. (1986), "Reverse-time migration of offset vertical seismic profiling data using the excitation-time imaging condition", *Geophysics*, **51**(1), 67-84.
- Lih, S. S. and Mal, A. K. (1995a), "On the accuracy of approximate plate theories for wave field calculations in composite laminates", *Wave Motion*, **21**(1), 17-34.
- Lih, S. S. and Mal, A. K. (1995b), "Response of multilayered composite laminates to dynamic surface loads", *Composite*, **27B**(6), 633-641.
- Lin, X. and Yuan, F. G. (2001a), "Damage detection of a plate using migration technique", *J. Intelligent Mater. Sys. Struct.*, **12**(7), 469-482.
- Lin, X. and Yuan, F. G. (2001b), "Detection of multiple damages by prestack reverse-time migration", *AIAA J.*, **39**(11), 2206-2215.
- Lin, X. and Yuan, F. G. (2001c), "Experimental study of applying migration technique in structural health monitoring", In: Chang, F.-K. (ed.), *Structural Health Monitoring: The Demands and Challenges*, CRC Press, USA, 1311-1320.
- Lin, X. and Yuan, F. G. (2005), "Experimental study applying a migration technique in structural health monitoring", *J. Struct. Health Monit.*, **4**(4), 341-353.
- Liu, P. L., Tsai, C. D. and Wu, T. T. (1996), "Imaging of surface-breaking concrete cracks using transient elastic wave", *NDT and E Int.*, **29**(5), 323-331.
- Sohn, H., Park, G., Wait, J. R., Limback, N. P. and Farrar, C. R. (2004), "Wavelet-based active sensing for delamination detection in composite structures", *Smart Mater. Struct.*, **13**(1), 153-160.
- Wang, L. and Yuan, F. G. (2005), "Damage identification in a composite plate using prestack reverse-time migration technique", *J. Struct. Health Monit.*, **4**(3), 195-211.